P8B.5

A NEW HIGH-ALTITUDE AIRBORNE MILLIMETER-WAVE RADAR FOR ATMOSPHERIC RESEARCH

Gordon Farquharson*, Eric Loew, Jothiram Vivekanandan, and Wen-Chau Lee
National Center for Atmospheric Research, Boulder, Colorado

1. INTRODUCTION

Clouds play an important role in the radiation budget for the earth-atmosphere system. To improve climate models, observations of cloud formation and associated dynamics are required. The recent launch of CloudSat (Stephens et al., 2002) will provide a wealth of information about clouds on a global scale. However, space-borne instruments are unable to provide simultaneous in situ measurements about the observed clouds, and thus, measurements from a combination of in situ sensors and airborne cloud radars are still necessary to study cloud processes.

Airborne millimeter wave radars have been used for atmospheric remote sensing since the early 1990s (Pazmany et al., 1994; Horie et al., 2000; Wolde and Pazmany, 2005), but most of the aircraft platforms on which these are borne lack a comprehensive a suite of in situ measurement capabilities. The National Center for Atmospheric Research has recently started operating a modified Gulfstream V aircraft, and has installed an array of sensors for atmospheric research (Laursen et al., 2006). The aircraft is called the High-Performance Instrumented Airborne Platform for Environmental Research (HIAPER) and is funded by the National Science Foundation (NSF). As part of the instrument suite for HIAPER, NSF is funding the development of the HIAPER Cloud Radar (HCR). The HCR will serve the atmospheric science research community by adding millimeter-wave remote sensing capabilities to the HIAPER aircraft. The HCR measurements in conjunction with other HIAPER instrumentation will provide the most complete picture of cloud physics available to atmospheric scientists. The HCR is scheduled for completion in 2009.

2. SYSTEM DESCRIPTION

The HIAPER Cloud Radar will be implemented in a phased approach. The first phase (Phase A) will consist of a single-polarimetric W-band (94 GHz) Doppler radar. Pulse compression and polarimetric capability will be added in Phase B, and Phase C will add a second wavelength (K_a-band) radar. In order to accommodate these extensions to the system, the Phase A system will be designed to accommodate the Phase B and C requirements.

The radar will be mounted in a 20 inch diameter (0.5 meter) wing pod. A conceptual drawing of the pod showing the major components is shown in Figure 1. A lens antenna is used to illuminate a rotatable reflector plate which allows the beam to be steered over almost 270 degrees from zenith through nadir in the plane normal to the fuselage of the aircraft. The radar front-end electronics (polarimetric switching network, LNAs, and calibration network) will be located directly behind the antenna. The transmitter and associated high power electronics, the intermediate frequency and receiver electronics, and the data system will be contained in a pressure vessel. The rest of the radar hardware (data storage, a real-time display, and a user interface) will be located in a 19 inch aircraft rack.

A block digram of the transceiver is shown in Figure 2. A digital waveform generator is used to control the spectral shape of the transmitted signal by applying an arbitrary amplitude taper or phase (frequency) coding. The output of the waveform generator is centered at 156.25 MHz, and is upconverted to 94.03125 GHz and amplified by an extended interaction klystron amplifier (EIKA). The directional coupler after the EIKA couples a small portion of the transmitted signal into the receiver through a well-calibrated attenuation network to measure changes in the absolute calibration. For this calibration scheme, knowledge of only the loss through the calibration path and the receive path before the LNA must be well characterized. This calibration scheme also allows for an adaptive pulse compression scheme to be implemented as a copy of the transmitted pulse is recorded. Measurements using a noise source or signal generators in the laboratory, or measurements of a corner reflector in the field will be required to determine the absolute calibration of the system. The receiver down-converts the received signal to a center frequency of 156.25 MHz. This intermediate frequency signal is sampled at a rate of 125 MS/s, which allows for a narrow- or a wide-band digital down-converter to be implemented in the digital receiver. The in- and quadrature-phase sampled will be sent by a gigabit Ethernet connection to the cabin for processing, display, and storage. All oscillators in the transceiver are phase locked to a 125 MHz stable oscillator. The 125 MHz signal is also used to generate the timing for the digital waveform generator and the data acquisition system.

A summary of the system parameters for the Phase A radar are listed in Table 1. The system will operate at 94.03125 GHz, with a peak radiated power of 900 W. The PRF and pulse length will be variable, but typical values of 10 kHz and 0.25 μs respectively are used in the simulations presented. For these parameters, the range resolution for the pulse length is 37.5 meters and the Nyquist velocity is ± 8 m s^{-1}. The beam width and gain of the antenna are 0.56 degrees and 48 dB respectively, and the receiver noise figure is 10 dB.

3. SYSTEM PERFORMANCE

The design of the HCR includes expansion to a fully-polarimetric dual-wavelength radar. The design analysis therefore covers not only the sensitivity and accuracy of the Phase A system, but also an analysis of the performance of polarimetric and dual-wavelength measurements.

* *Corresponding author address:* Gordon Farquharson, NCAR/EOL, 1850 Table Mesa Dr., Boulder, CO 80305; e-mail: gordonf@ucar.edu

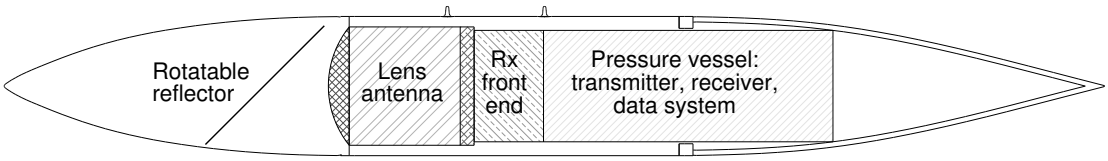

Figure 1: Side view of the 20" HIAPER wing pod showing the layout of the radar electronics. The front of the pod is on the left hand side of the figure. The reflector plate is positioned such that the beam clears the leading edge of the wing when pointing vertically.

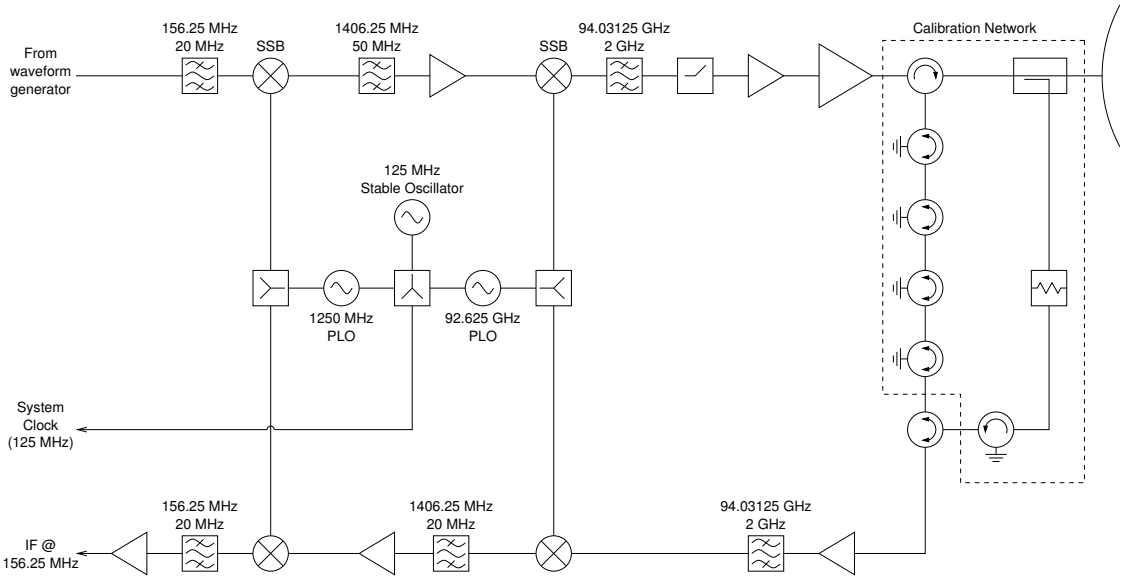

Figure 2: Block diagram of the radar transceiver. All oscillators are phase locked to the 125 MHz oscillator.

Table 1: System Parameters

Frequency	94 GHz
Peak radiated power	900 W
PRF	10 kHz
Pulse width	0.25 μs
Antenna gain	48 dB
Receiver noise figure	10 dB

3.1 Sensitivity

The minimum detectable reflectivity for Rayleigh scattering as a function of range from the radar is calculated from

$$Z = 10^{18} \frac{2^{10} \log(2) \lambda^2 l_r}{\pi^3 P_t G_a^2 c \tau \theta_b K_w^2} P_n R^2 \sqrt{2/M_I} \qquad (1)$$

where λ is the wavelength, l_r is the loss due to the finite bandwidth of the receiver, P_t is the transmitted (radiated) power, G_a is the antenna gain, c is the speed of light, τ is the pulse length, θ_b is the antenna beam width, K_w^2 is the related to the refractive index of water, P_n is the system noise power, R is the range from the radar, and M_I is the number of independent samples.

The minimum detectable reflectivity at 0 dB SNR is calculated by using the a mid-latitude summer profile of pressure, temperature and water vapor density (top three panels of Figure 3). The atmospheric attenuation due to oxygen and water vapor is then calculated using the Millimeter-wave Propagation Model (MPM93, Liebe et al. (1993)) as a function of height from the profile data (lower left-hand panel in Figure 3). The attenuation profile is integrated to determine the cumulative attenuation as a function of range for a radar at 12 km altitude (lower middle panel in Figure 3), and the minimum detectable reflectivity (lower right-hand panel in Figure 3) is calculated using Equation 1 for each range assuming a 120 ms dwell time and a background brightness temperature of 300 K. A 120 ms dwell corresponds to 28 meters along the flight track at the long-range cruising speed (236 m s-1) of the aircraft.

Minimum detectable reflectivity for a vertical profile are tabulated for specific ranges in the second row of Table 2. The third row shows the minimum detectable reflectivity for a horizontal profile at an altitude of 10 km, assuming a 62 K background temperature. A significant difference in the sensitivity of the radar only occurs within the boundary layer where the concentration of water vapor increases the attenuation of the electromagnetic wave.

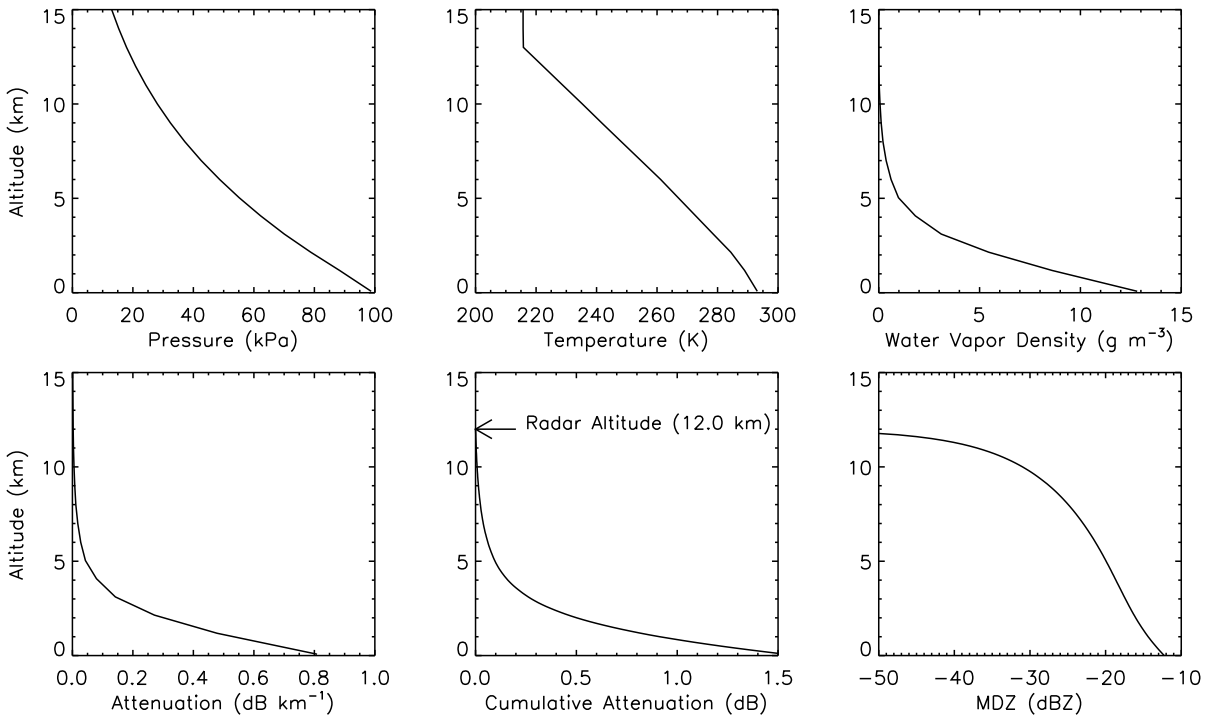

Figure 3: Simulated minimum detectable reflectivity for a vertical profile. The radar is at an altitude of 12 km.

Table 2: Minimum detectable reflectivity for a 0 dB SNR and integration over a 120 ms dwell time

Range (km)	1	2	5	10	12
MDZ (vertical profile from 12 km)	−37	−31	−23	−17	−12
MDZ (horizontal profile at 10 km)	−37	−31	−23	−17	−16

Table 3: Standard deviation in reflectivity measurement (dB)

	Spectral Width (m s^{-1})				
SNR (dB)	0.25	0.5	1	1.5	2
0	0.44	0.40	0.34	0.30	0.29
10	0.39	0.34	0.26	0.22	0.19
20	0.39	0.33	0.26	0.21	0.19
30	0.39	0.33	0.26	0.21	0.19

3.2 Reflectivity Accuracy

The standard deviation in reflectivity ΔZ_{dB} for a Gaussian Doppler spectrum is approximately given by (Doviak and Zrnić, 1993; Hogan et al., 2005)

$$\Delta Z_{\text{dB}} = \frac{10\log_{10}(e)}{\sqrt{MN}}\left(\frac{\lambda}{4\pi^{(1/2)}\sigma_w\tau_s}+\frac{1}{\text{SNR}^2}+\frac{2}{\text{SNR}}\right)^{(1/2)} \quad (2)$$

where M is the number of pulse repetition intervals in the dwell time, N is number of ranges gates averaged, SNR is the linear signal to noise ratio, τ_s is the pulse repetition time, σ_w is the spectral width of the scatterers. For a dwell time of 120 ms, a PRF of 10 kHz, and averaging over one range gate, the standard deviation in reflectivity varies from 0.44 to 0.19 dB for signal to noise ratios of 0 to 30 dB and spectral widths of 0.25 to 2 m s^{-1} (Table 3).

3.3 Polarimetric Measurements

A reflector plate will be used to steer the antenna beam. The reflector plate changes the polarization of the transmitted waveform as it rotates, which therefore changes the basis in which polarimetric variables are measured. Consider an incident electric field polarized in the $\hat{x}$ direction and propagating in the $+\hat{z}$ direction ($\vec{E}^i = \hat{x}E_0^i e^{-jk_0 z}$). If the reflector plate is rotated counterclockwise around the z-axis by an angle ψ, then the electric field reflected by the plate is

$$\vec{E}^r = E_0^i\left\{-\hat{x}\sin^2\psi - \hat{y}\cos\psi\sin\psi - \hat{z}\cos\psi\right\} \times e^{-jk_0(x\cos\psi - y\sin\psi)}. \quad (3)$$

The relationship between these vectors is illustrated in Figure 4 where $\xi = \cos^{-1}\left(\cos\psi\sin^2\psi + cos^2\psi\right)$. Because of this change in polarization, measurements made while scanning will necessitate a rotation of the polarimetric variables to a common polarimetric basis. However, the transformation to a common basis induces an error in the measured polarimetric variables due to the limited cross-polarimetric isolation of the radar. This error is studied through the use of a simple model which is presented next.

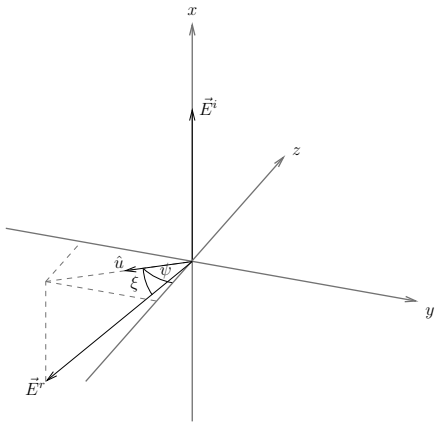

Figure 4: Incident and reflected electric field vectors in the xyz coordinate system. The incident electric field vector is vertical with respect to the aircraft frame of reference, and the reflected electric field vector rotates in azimuth and elevation for a rotation of the reflector plate. The reflector plate has a counter-clockwise rotation ψ from the point of view of the antenna.

The cross-polarimetric isolation I in decibels for the antenna and orthomode transducer (OMT) is modeled as a single number ε where

$$\varepsilon = 10^{-I/20} \,. \tag{4}$$

The HCR will use alternating polarimetric transmitted waveforms to measure the full polarimetric matrix. If transmitted signal amplitude is M, the radiated signal amplitudes for transmit H-polarization and transmit V-polarization ($\hat{h}\hat{v}$ basis) are

$$\vec{M}_h = \begin{bmatrix} 1-\varepsilon \\ \varepsilon \end{bmatrix} \text{ and } \vec{M}_v = \begin{bmatrix} \varepsilon \\ 1-\varepsilon \end{bmatrix} \tag{5}$$

respectively. The amplitude of the received signals at the antenna are

$$\vec{V}^{10} = \mathbf{S}\vec{M}_h \text{ and } \vec{V}^{01} = \mathbf{S}\vec{M}_v \tag{6}$$

where $\mathbf{S}$ is the scattering matrix describing the atmospheric state, and $\vec{V}^{10}$ and $\vec{V}^{01}$ are the received signals at the antenna for transmit H-polarization and transmit V-polarization respectively. The amplitudes of these signals at the input to the H- and V-channel receivers (after the antenna and OMT which have limited cross-polarimetric isolation) are

$$\begin{aligned} \vec{V}_r^{10} &= \begin{bmatrix} V_{\text{co}}^{10} \\ V_{\text{cr}}^{10} \end{bmatrix} = \begin{bmatrix} 1-\varepsilon & \varepsilon \\ \varepsilon & 1-\varepsilon \end{bmatrix} \vec{V}^{10} \text{ and} \\ \vec{V}_r^{01} &= \begin{bmatrix} V_{\text{cr}}^{01} \\ V_{\text{co}}^{01} \end{bmatrix} = \begin{bmatrix} 1-\varepsilon & \varepsilon \\ \varepsilon & 1-\varepsilon \end{bmatrix} \vec{V}^{01} \,, \end{aligned} \tag{7}$$

and therefore the measured S-parameter matrix is

$$\mathbf{S_m} = \begin{bmatrix} V_{\text{co}}^{10} & V_{\text{cr}}^{01} \\ V_{\text{cr}}^{10} & V_{\text{co}}^{01} \end{bmatrix} \,. \tag{8}$$

The S-parameter matrix and the measured signals are transformed to the common orthogonal polarimetric basis ($\hat{h}'\hat{v}'$) through a rotation matrix $\mathbf{R}$ where

$$\mathbf{R} = \begin{bmatrix} \cos\chi & \sin\chi \\ -\sin\chi & \cos\chi \end{bmatrix} \tag{9}$$

where $\chi = \hat{h}\cdot\hat{h}'$ is the angle between the polarimetric bases measured from the h axis. The S-parameter matrix describing the atmospheric state in the $\hat{h}'\hat{v}'$ basis is

$$\mathbf{S}' = \mathbf{RSR}^{-1} \,, \tag{10}$$

and the measured S-parameters are

$$\mathbf{S}'_{\mathbf{m}} = \mathbf{RS_mR}^{-1} \,. \tag{11}$$

An example scattering matrix (Equation 12) describing the atmosphere is assumed to obtain numerical results from this model.

$$\mathbf{S} = \begin{bmatrix} 0.9 & 0 \\ 0 & 0.8 \end{bmatrix} \tag{12}$$

The effect of limited cross-polarimetric isolation when transforming to a common basis is shown by plotting the actual and measured differential reflectivity (Z_{dr}) and linear polarization ratio (LDR) versus the the angle of rotation χ between the basis sets and for a cross-polarimetric isolation of 30 dB (Figure 5). The difference between the actual and measured Z_{dr} values increases from 0 up to around 1.2 dB as the rotation angle increases from 0 to 45 degrees and then returns to 0 dB at 90 degrees because the transmitted basis is aligned with the common basis again at 90 degrees. The actual LDR at 0 degrees rotation is $-\infty$ whereas the measured LDR is -24.2 dB due to the finite cross-polarimetric isolation of the OMT and antenna. The difference varies as the rotation angle increases. At 90 degrees, the measured LDR is the same as at 0 degrees, as expected. Thus, a correction based on the cross-polarimetric isolation will need to be applied to the measured polarimetric variables when transforming to a common polarimetric basis.

3.4 Cloud Liquid Water Content Measurements

In general, single-wavelength retrievals of liquid water content (LWC) cannot be estimated accurately from reflectivity (Vivekanandan et al., 1999). For example, for Rayleigh scattering, LWC can vary from 0.2 to 0.7 g m^{-3} when the reflectivity is -10 dBZ. However, if the drop size distribution of the clouds is measured with in situ probes on HIAPER, it may be possible to generalize the retrieval to the rest of the cloud using the reflectivity measurement.

Dual-wavelength measurements from the Phase C system will provide a more accurate retrieval than the single-wavelength retrieval. The standard deviation in mean LWC in a layer between heights h_1 and h_2 is directly related to the uncertainty in radar reflectivity (Hogan et al., 2005) and is given by

$$\Delta\text{LWC} = \frac{\left(\Delta Z_{35}^2 + \Delta Z_{94}^2\right)^{(1/2)}}{\sqrt{2}\left(\kappa_{94} - \kappa_{35}\right)\left(h_2 - h_1\right)} \tag{13}$$

where ΔZ_{35}^2 and ΔZ_{94}^2 are the variance in reflectivity at 35 and 94 GHz respectively, and κ_{94} and κ_{35} are the one-way specific attenuation coefficients of liquid water in dB km^{-1} (g m^{-3})$^{-1}$ for 94 and 35 GHz respectively.

The specific attenuation of liquid water calculated using MPM93 is 1.298 dB km^{-1} (g m^{-3})$^{-1}$ at 35 GHz and 4.568 dB km^{-1} (g m^{-3})$^{-1}$ at 94 GHz for a pressure of 700 mb and a temperature of -10°C. Assuming that both the 35 and

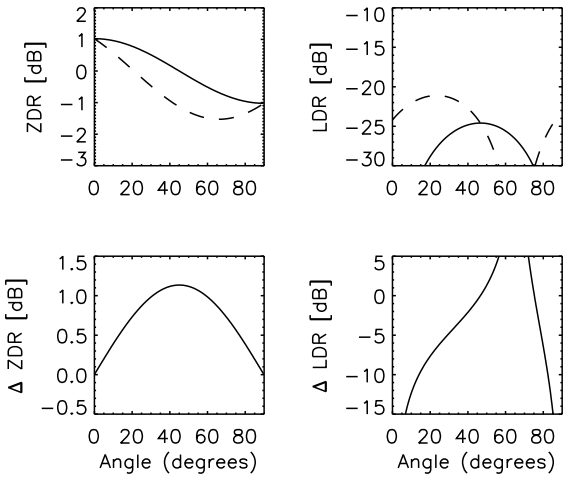

Figure 5: The top left-hand plot shows the actual (solid) and measured (dashed) values of Z_{dr} versus rotation angle for a cross-polarimetric isolation of 30 dB. The bottom left-hand plot shows the difference in actual and measured Z_{dr}. The top right-hand plot shows the actual (solid) and measured (dashed) values of LDR versus rotation angle for a cross-polarimetric isolation of 30 dB. The bottom right-hand plot shows the difference in actual and measured LDR.

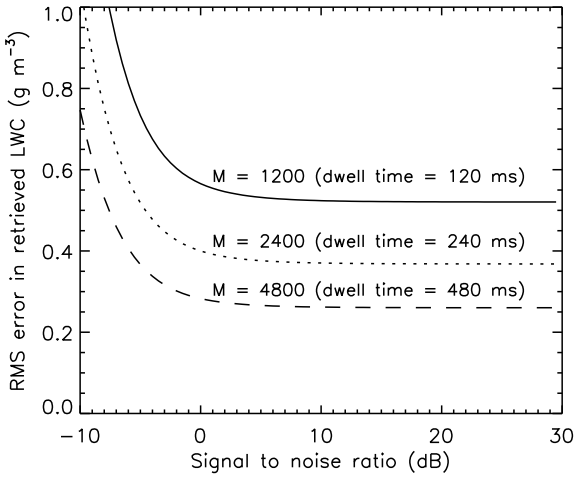

Figure 6: Predicted LWC error from dual-wavelength (35 and 94 GHz) measurements as a function of signal to noise ratio for dwell times of 120, 240, and 480 ms.

94 GHz have the same signal to noise ratio, pulse repetition frequency, and assuming that the spectral width of the scatterers is the same, the standard deviation in LWC versus signal to noise ratio can be plotted for various dwell times (Figure 6). In this simulation, four resolution gates are averaged, and the standard deviation in velocity of the scatterers is 0.5 m s^{-1}.

The standard deviation in liquid water content for these parameters varies from 0.26 g m^{-3} to 0.52 g m^{-3} for dwell time from 480 to 120 ms and signal to noise ratios above 0 dB. LWC concentration that is typically found in stratocumulus clouds (< 1 g m^{-3}) is on the order of the accuracy achievable with the system configuration only for dwell times greater than 480 ms. This time corresponds to 96 meters along the track of the aircraft at 200 m s^{-1}, which depending on the homogeneity of the clouds under being studied, may be sufficient to make a useful retrieval.

ACKNOWLEDGMENT

The National Center for Atmospheric Research is sponsored by the National Science Foundation. The views expressed are those of the authors and do not necessarily represent the official policy of the U.S. government.

REFERENCES

Doviak, R. J. and D. S. Zrnić, 1993: *Doppler Radar and Weather Observations*. Academic Press, second edition.

Hogan, R. J., N. Gaussiat, and A. J. Illingworth, 2005: Stratocumulus liquid water content from dual-wavelength radar. *J. Atmos. Oceanic Technol.*, **22**, 1207–1218.

Horie, H., T. Iguchi, H. Hanado, H. Kuroiwa, H. Okamoto, and H. Kumagai, 2000: Development of a 95-GHz airborne cloud profiling radar (SPIDER) - Technical aspects. *IEICE Trans. Comm.*, **E83B**, 2010–2020.

Laursen, K. K., D. P. Jorgensen, G. P. Brasseur, S. L. Ustin, and J. Hunning, 2006: HIAPER: The next generation NSF/NCAR research aircraft. *Bulletin of the American Meteorological Society*, **87**, 896–909.

Liebe, H. J., G. Hufford, and M. Cotton, 1993: Propagation modeling of moist air and suspended water/ice particles at frequencies below 1000 ghz. *Proc. of 52nd Specialists meeting of the Electromagnetic Wave Propagation Panel*, AGARD, 542.

Pazmany, A. L., R. E. McIntosh, R. Kelly, and V. G., 1994: An airborne 95-GHz dual-polarized radar for cloud studies. *IEEE Trans. Geosci. Remote Sens.*, **32**, 731–739.

Stephens, G., D. G. Vane, R. J. Boain, G. Mace, K. Sassen, Z. E. Wang, A. J. Illingworth, E. J. O'Connor, W. B. Rossow, S. Durden, S. Miller, R. T. Austin, A. Benedetti, and C. Mitrescu, 2002: The cloudsat mission and the A-train – A new dimension of space-based observations of clouds and precipitation. *Bulletin of the American Meteorological Society*, **83**, 1771–1790.

Vivekanandan, J., B. E. Martner, M. K. Politovich, and G. F. Zhang, 1999: Retrieval of atmospheric liquid and ice characteristics using dual-wavelength radar observations. *IEEE Trans. Geosci. Remote Sens.*, **37**, 2325–2334.

Wolde, M. and A. Pazmany, 2005: NRC dual-frequency airborne radar for atmospheric research. *32nd Int. Conf. on Radar Meteor.*, AMS.